

Raman Microspectroscopy of a Multi-Crystalline Silicon Solar Cell

Jeya Prakash Ganesan , Nafis Iqbal , Milos Krsmanovic , Fernand Torres-Davila , Andrew Dickerson, Kristopher O. Davis , Laurene Tetard, and Parag Banerjee 

I. INTRODUCTION

Abstract—A multicrystalline silicon solar cell was analyzed using Raman microspectroscopy. We measured the prominent Raman modes of silicon, nanocrystalline silicon and silver oxide in various regions of the solar cell to generate insights into the process and material quality of the finished device. First, by comparing the distribution of the transverse optical (TO) phonon peak position and full-width-at-half-maximum (FWHM) of the solar cell with a single crystal silicon wafer, the quality of the multicrystalline silicon surface was ascertained. Second, a similar analysis of the remnant saw marks on the device surface showed a discernably higher and wider distribution of TO phonon peak position and FWHM compared to a multicrystalline silicon surface. This indicated the presence of residual compressive stresses in the saw mark region. Third, by observing the silver fingers and bus bars, a residual silver oxide layer was identified, up to 25 μm away from the line edges. This was attributed to the screen printing of the silver paste and the subsequent firing process. Finally, Raman mapping on an embedded inclusion showed the presence of nanocrystalline silicon phase. The multicrystalline silicon region surrounding the inclusion was under tensile stress. A nondestructive, confocal Raman analysis of the inclusion provided a 3-D visualization of the defect, both inside and above the surface of the multicrystalline silicon wafer.

Index Terms—Back surface field (BSF), confocal Raman, photovoltaics.

Manuscript received June 13, 2021; revised September 17, 2021; accepted October 29, 2021. Date of publication November 25, 2021; date of current version December 23, 2021. This work was supported by the National Science Foundation (NSF) under Award 1922984 and use of HORIBA LabRam[®] confocal Raman is possible with support from NSF MRI under Award 1920050. (Corresponding authors: Laurene Tetard; Parag Banerjee.)

Jeya Prakash Ganesan and Nafis Iqbal are with the Department of Materials Science and Engineering, University of Central Florida, Orlando, FL 32816 USA (e-mail: jeyaprakashganesan@knights.ucf.edu; nafisiqbal@knights.ucf.edu).

Milos Krsmanovic and Andrew Dickerson are with the Department of Mechanical and Aerospace Engineering, University of Central Florida, Orlando, FL 32816 USA (e-mail: milos@knights.ucf.edu; andrew.dickerson@ucf.edu).

Fernand Torres-Davila is with the Department of Physics and Astronomy and Nanoscience Technology Center, University of Central Florida, Orlando, FL 32816 USA (e-mail: fernand.torres@knights.ucf.edu).

Kristopher O. Davis is with the Department of Materials Science and Engineering, Florida Solar Energy Center and Resilient, Intelligent and Sustainable Energy Systems, Faculty Cluster Initiative, University of Central Florida, Orlando, FL 32816 USA (e-mail: kristopher.davis@ucf.edu).

Laurene Tetard is with the Department of Physics and Astronomy, Nanoscience Technology Center and Renewable Energy and Chemical Transformation, Faculty Cluster Initiative, University of Central Florida, Orlando, FL 32816 USA (e-mail: laurene.tetard@ucf.edu).

Parag Banerjee is with the Department of Materials Science and Engineering, Florida Solar Energy Center, Nanoscience Technology Center and Renewable Energy and Chemical Transformation, Faculty Cluster Initiative, University of Central Florida, Orlando, FL 32816 USA (e-mail: parag.banerjee@ucf.edu).

Color versions of one or more figures in this article are available at <https://doi.org/10.1109/JPHOTOV.2021.3126106>.

Digital Object Identifier 10.1109/JPHOTOV.2021.3126106

TECHNOLOGICAL advances in solar cell manufacturing at economies-of-scale have led to a significant decrease in the price of solar cells. Additionally, new materials and improved processes have steadily led to the increase of solar cell efficiencies [currently at 26.7% for silicon (Si) solar cells] and reliability [20 years with < 5.6% degradation in open-circuit voltage (V_{oc})] [1]–[3]. Consequently, costs for energy generation using Si solar cells have dropped to 0.038 \$/kW-hr, which puts it at par with other sources of non-renewables such as, coal (0.12 \$/kW-hr) and hydroelectric (0.039 \$/kW-hr) [4]. Si solar cells capture a significant portion (90%) of the solar cell market [5]. The high-volume manufacturing environments for Si solar cells integrate processes that dope precise regions in the absorber layers, create textured surfaces that efficiently absorb solar irradiation, integrate transparent conductors and metallic films onto the device, while packaging, wiring and laminating cells into modules [6]. Today, the Si solar cell is a complex stack of materials with specific electrical, optical, structural, and mechanical functionalities.

For continued cost and efficiency gains, characterization tools play a critical role. With the right modality of measurement, minute variations in materials quality can be detected. Techniques that are currently used include optical inspection and electrical testing. However, these techniques measure performance at the macroscale (i.e., module level) and either lack the sensitivity or spatial resolution to map materials quality variations within a solar cell [7].

We posit that Raman microspectroscopy offers many advantages for the characterization of Si-based solar cells. The Raman instrumentation is affordable, no special sample preparation is required, and measurements can be conducted in ambient conditions. The Raman spectrum for Si exhibits a pronounced transverse optical (TO) phonon mode centered at $\sim 520 \text{ cm}^{-1}$ which is easily detected [8]. The peak position and full-width-at-half-max (FWHM) are indicators of Si crystalline quality and contain stress information [9]. Other materials used in Si solar cells such as, transparent oxide conductors [10]–[12] and interfacial layers of oxides produce their own Raman signal and thus, chemical mapping is possible. Importantly, coupling Raman with confocal measurements (in the Z , i.e., depth direction) can lead to a modality which is non-destructive and provides microscale sub-surface information [13]. This is a clear advantage that Raman has over other characterization techniques

used to study Si-based solar cells. Finally, the optics of the microscope and the laser wavelength plays an important role in determining the X , Y and Z resolution of the measurements and micrometer scale lateral resolution is routinely possible. However, Raman microspectroscopy is currently *not* optimized for Si solar cell characterization. The measurements are slow and usually take several minutes to be acquired. With proper hardware modifications including use of multiple heads, faster raster scans and optimized signal acquisition algorithms, it is possible to acquire data in time scales which are well within the requirements of high-volume solar cell manufacturing environments.

There have been a few reports on the use of Raman on Si solar cells. Beinert *et al.* [14] showed that the front glass in a laminated mono crystalline Si solar cell has no influence on the stress measurements through confocal Raman. The measured Raman results agree with the simulated finite-element modeling results. Gundel *et al.* [15] reported the use of micro-Raman and microphotoluminescence in determining the doping density and carrier recombination lifetime in a multicrystalline Si solar cell. Pogue *et al.* [16] showed that the wire sawing techniques produce residual compressive stresses in the as-cut multicrystalline Si wafers through micro-Raman spectroscopy. Becker *et al.* [17] showed that through Raman spectroscopy, stress tensor components within grains of arbitrary orientations in a polycrystalline Si solar cell can be measured. However, most of the reports focused on the primary material of the solar cell, Si for characterization.

Here, we report the use of Raman microspectroscopy to characterize multiple materials (e.g., Si, nanocrystalline Si, silver oxide), inside a fully finished, textured, multicrystalline Si solar cell. The fully finished solar cell is a stack of heterogeneous materials. A variety of processes have been integrated together to form the final device and therefore, process interdependencies play a role in the final quality of the material. We focus on the Raman mapping [2-D i.e., XY and 3-D i.e., XYZ] of regions with observable defects, such as remnants of saw marks on the Si surface, edges of the silver fingers and particle inclusions.

We establish that it is possible to ascertain the quality of the Si substrate of the solar cell; see differences in crystalline quality of textured Si surfaces with and without remnant saw marks; observe silver (Ag) lines containing a, hitherto unreported, region of silver oxide (Ag_2O) extending tens of micrometers over the active region; and identify inclusions embedded inside the substrate as nanocrystalline Si—possibly a leftover swarf from the sawing process. Thus, we demonstrate the broad utility of Raman microspectroscopy in providing insights into the surface and subsurface quality of the textured solar cell, the condition of the silver contacts, and the nature of an inclusion embedded in a solar cell.

II. EXPERIMENTAL DETAILS

Multicrystalline aluminum back surface field (Al-BSF) solar cell was obtained from Canadian Solar. From top to bottom, the layers were Ag contacts, a 75 nm SiN_x layer as an antireflecting coating (ARC), n -type Si as emitter, 180 μm p -type Si absorber

and a thick 250- μm thick Al back contact. Optical images for profilometry were taken using a Keyence Digital Microscope VHX-5000. The instrument used to perform XY micro-Raman spectroscopy was a WITec 300 RA microscope. The mappings were performed using a laser excitation radiation of 532 nm. The penetration depth of this laser in Si is $\sim 1.27 \mu m$ [18]. With the 20 \times objective used, the optical system provides a depth of focus (DOF) of 7 μm and a spot radius of 400 nm.

It is important to verify that the laser power from the Raman microscope does not lead to temperature changes in the Si substrate. This is because an increase in temperature leads to a corresponding decrease in the TO phonon peak position of Si and thus, erroneous conclusions can be drawn [19]. We have studied the combined impact of laser power *and* temperature on the TO phonon peak position of single crystalline Si for the WITec system. This is shown in supporting information S1. Briefly, a single crystal, p -type (100) Si wafer was placed on a heated stage under the Raman microscope and the temperature was varied as 25 $^\circ C$, 50 $^\circ C$, 75 $^\circ C$, 100 $^\circ C$, and 125 $^\circ C$. At each temperature, the laser power was varied as 4.4, 13.5, 24.3, and 32 mW. It was found that the temperature played a far critical role in lowering the TO phonon peak position wavenumber, from 520.3 to 518 cm^{-1} . At any given temperature, increasing laser intensity did not result in a measurable shift in the TO phonon peak, indicating that the laser power did not cause any significant change in the temperature of the illuminated region of sample over and above the temperature of the substrate.

The spot radius of 400 nm also provides the necessary information for conducting XY mapping. For example, an area of $25 \times 25 \mu m^2$ was mapped with a grid size of 31×31 (i.e., a total of 961 data points) with each step 800 nm apart which is equal to the spot diameter. The laser intensity used was 6 mW. Unless otherwise noted, the accumulation time was 1 s and every scan was integrated once. A larger area scan of $75 \times 25 \mu m^2$ with 2852 data points was performed with an objective of 20 \times on saw marks. The laser intensity used was 20 mW. For the Ag finger a lower magnification using a 10 \times objective was used, an area of $140 \times 140 \mu m^2$ was mapped with 2500 data points. The laser intensity used was 30 mW. For the inclusion, an objective of 10 \times was used on an area of $45 \times 45 \mu m^2$ mapped with 784 data points. The accumulation time was 2 s, and every scan was integrated once. The laser intensity used was 25 mW. Scan acquisition was conducted from 12 to 1200 cm^{-1} wavenumbers using a grating with 1800 gratings/mm and a resolution of 0.3 cm^{-1} . Total accumulation times for obtaining area scans ranged from tens of minutes to up to 3 h long.

To achieve true confocal imaging of the inclusion reported in this article, a Horiba LabRam Evolution system with a 785 nm laser was used. This laser wavelength allows for a penetration depth of 10 μm [18]. The experimental conditions for confocal mapping were 1 s integration time and 1 accumulation. A 50 \times long working distance objective, 1800 gratings/mm and a laser intensity of 25 mW was used to conduct the 3-D mapping. The total measurement time to collect all 36 938 spectra was 14 h. Prior to conducting any Raman measurements, the equipment were calibrated using a pristine, single crystal Si wafer with the TO phonon adjusted to 520.5 cm^{-1} .

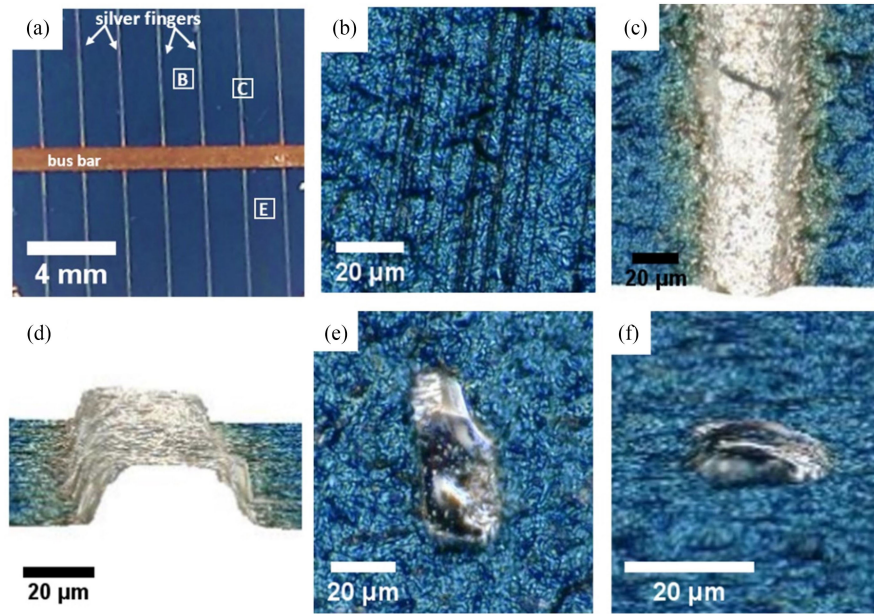


Fig. 1. (a) Surface image of a multicrystalline solar cell. Bus bar and Ag fingers are labeled. Regions marked B, C, and E correspond to approximate regions for scratch mark, Ag finger and inclusion, respectively. (b) Optical profilometer image of scratch marks. (c) Optical profilometer image of Ag finger. (d) 3-D cross-section of the Ag finger region. (e) Optical profilometer image of inclusion. (f) 3-D cross-section image of the inclusion.

Postprocessing of data including background subtraction and noise reduction through data averaging techniques were conducted with the instrument's proprietary software. Where necessary, data was exported as text files and custom-built MATLAB codes were written to extract the relevant information. These exceptions to data analyses will be described individually before the relevant results. As a clarification, Raman peak intensity maps imply mapping the height of the Raman peak.

III. RESULTS AND DISCUSSION

Fig. 1(a) shows the surface image of the multicrystalline solar cell. The presence of Si nitride (Si_3N_4) as an ARC makes the surface appear blue in color. Screen printed Ag fingers are approximately 2 mm apart. Regions marked on this image were analyzed using Raman microspectroscopy and will be described next. Region "B" is the approximate region where remnants of saw marks were visible. Region "C" indicates the Ag finger on the solar cell coupon. Region "E" marks the presence of an inclusion found on the Si surface between two Ag fingers.

Fig. 1(b) shows the saw mark region "B." These saw marks appear to run parallel to each other, characteristic of the wire-saw based process employed for wafering. Usually, saw marks are removed during the surface texturing process. However, in this case, a small region ($\sim 2 \text{ mm}^2$) still shows remnant saw marks on the multicrystalline Si surface. Fig. 1(c) shows the top down and, Fig. 1(d) shows the profilometric cross section of the Ag finger. The cross section of the Ag finger is approximately rectangular in shape. The fingers are $\sim 30 \mu\text{m}$ wide and $\sim 10 \mu\text{m}$ tall. The sidewalls are slightly tapered with an angle of 60° . Next to the sidewalls there appears to be a planar, "spill-over" region that has leftover Ag from the firing process which is described in detail below. Fig. 1(e) and (f) shows the optical

profilometry image of the inclusion present on the Si surface. The inclusion measures $20 \mu\text{m}$ in the X-direction, $45 \mu\text{m}$ in the Y-direction.

Fig. 2(a) shows the Raman spectrum obtained on the multicrystalline Si solar cell surface. The TO phonon peak is centered at 520.3 cm^{-1} . The inset shows the micrograph of the textured Si surface acquired under the microscope at a magnification of $20\times$. The $25 \times 25 \mu\text{m}^2$ red boxed region is mapped next. Fig. 2(b) shows the XY contour plot of the variation of Raman peak intensity. The variation in intensity on the multicrystalline Si surface is attributed to the texturing process that causes the variation in the Si surface topology. Thus, regions in the plane of focus cause higher peak intensities. Regions away from the plane of focus (either above or below) cause lower peak intensities. The distribution of the peak position in a $25 \times 25 \mu\text{m}^2$ area is shown in Fig. 2(c). A MATLAB code was written to extract the peak position and FWHM using a Lorentzian fit. Recall that a total of 961 data points were acquired for this area scan. The peak position varies from 520.2 to 520.6 cm^{-1} and follows a Gaussian distribution. The peak position distribution of a multicrystalline solar cell is overlaid over the peak position distribution of a pristine, single crystal Si wafer and appear to be very similar. The similarity in the distributions indicates similarity in the crystalline quality of Si between both samples. Since peak positions are also indicative of mechanical stress in Si [20], these results indicate that the multicrystalline Si is stress free in the red boxed region of Fig. 2(a). As a further confirmation of this conclusion, in Fig. 2(d) the variation of FWHM of the Si peak is overlaid over the variation of FWHM of the pristine single crystal Si wafer. This variation is found to be in the range 2.7 to 3.8 cm^{-1} for both samples. Polycrystallinity and grain boundary effects were not observed on the multicrystalline Si surface.

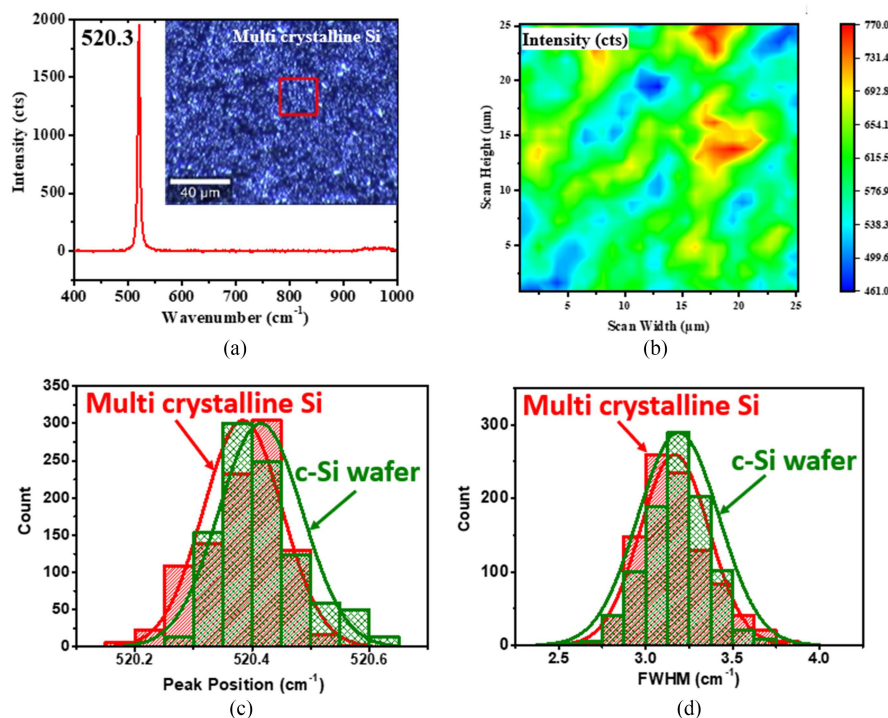


Fig. 2. (a) Si Raman spectrum of the TO phonon peak centered at 520.3 cm^{-1} . The inset shows the surface of the textured multicrystalline Si solar cell surface. (b) Intensity map of a $25 \times 25 \text{ mm}^2$ red box from (a) which contains 961 data points. (c) and (d) Histogram distribution of peak position (c) and FWHM (d) of the multicrystalline Si compared with a single crystal.

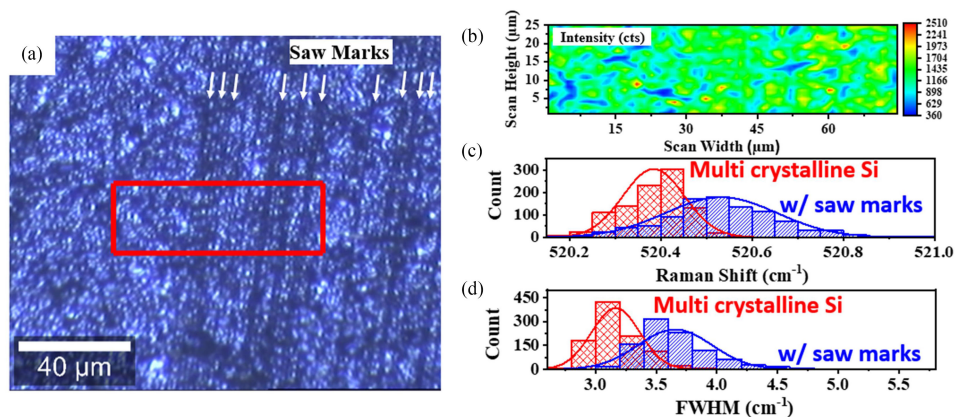


Fig. 3. (a) Region of Si solar cell indicating saw marks. The $75 \times 25 \text{ mm}^2$ red box is the region in which Raman mapping was conducted. (b) Contour plot of Raman intensity shows no indication of the saw marks. (c) and (d) Distribution of peak position (c) and FWHM (d) from area mapping for multicrystalline Si only and Si with saw marks regions.

Fig. 3(a) shows the micrograph of saw marks present on the Si. As stated before, the saw marks are suspected to be remnants of an incomplete etching and texturing process which otherwise should have removed the imperfections from the surface. The red boxed region measuring $75 \times 25 \text{ } \mu\text{m}^2$ was mapped under the Raman microscope next. Fig. 3(b) shows the XY contour plot of the intensity of the Si. It is interesting to note that the saw marks do not register on the intensity plot. This is possibly a result of the textured surface determining the surface topology of the multicrystalline Si. Fig. 3(c) and (d) shows the distribution of the peak position and the FWHM of the Si peak,

respectively. A MATLAB code was written to extract the peak position and FWHM using a Lorentzian fit. These are overlaid with the distribution of peak position and FWHM from the multicrystalline textured Si shown in Fig. 2(c) and (d). It is important to note that since the areal mapping of the saw marks region is larger ($75 \times 25 \text{ } \mu\text{m}^2$) than the region without saw marks evaluated previously in Fig. 2 ($25 \times 25 \text{ } \mu\text{m}^2$), the histogram for the saw marks were sampled to match the size of the evaluated region without saw marks, i.e., $25 \times 25 \text{ } \mu\text{m}^2 = 961$ data points. Both the peak position and the FWHM are shifted to a higher value for the saw marks region, indicating that in the presence

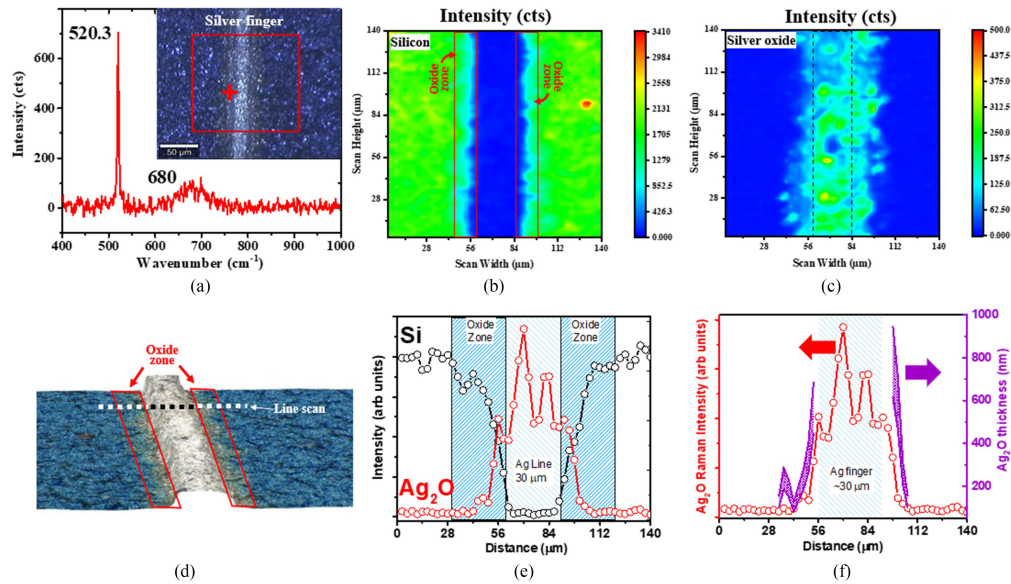


Fig. 4. (a) Raman spectrum of the silver line on the “+” mark in the inset shows two peaks—one at 520.3 cm^{-1} corresponding to the underlying Si and another, weaker peak at 680 cm^{-1} which corresponds to Ag_2O . (b) Contour plot of the intensity of 520.3 cm^{-1} peak shows the presence of Si around the silver line. The “oxide” zone is labeled which shows diminished Si intensity. (c) Intensity of the 680 cm^{-1} peak is shown which appears concentrated above and in the vicinity of the silver line. (d) 3-D profilometer image shows the oxide zone and the dotted lines are approximate positions of representative Si and Ag_2O line scans which are provided as intensity plots in (e) and (f), respectively. From the drop in Si intensity and, assuming the absorption coefficient for Ag_2O to lie between 0.00078 and 0.0012 nm^{-1} it is possible to estimate the thickness of Ag_2O in the oxide zone.

of the saw marks the Si is under compressive stress. Similar Raman shifts indicating residual compressive stress have been reported when analyzing Si swarf from the sawing process [21]. Further, the peak position and FWHM distributions are wider for the saw marks region. FWHM are an indicator of the crystalline quality of the Si and performing statistical analysis of Raman data helps to delineate these differences. It is to be noted that the silicon nitride layer on top of the silicon surface may affect the stress of the underlying Si. However, by comparing the silicon regions with and without the saw marks the compressive stress originating from the nitride layer (which is common to both the regions) can be eliminated.

Fig. 4(a) shows a single Raman spectrum at the edge of the Ag finger shown in the inset with a “+” mark. The spectrum consists of two peaks. The primary peak is the TO phonon belonging to Si at 520.3 cm^{-1} and the weaker, broader peak is at 680 cm^{-1} . The peak at 680 cm^{-1} is attributed to the vibration of $\text{Ag}[\text{O}-\text{O}]^2$ bond in Ag_2O [22]. The origin of Ag_2O can be attributed to oxidation of Ag during the firing process [23], [24].

Fig. 4(b) shows the areal mapping of the Si peak intensity from the red boxed region in the inset of Fig. 4(a). At distances $\geq 15\text{ }\mu\text{m}$ from the edge of the Ag line, the Si peak intensity is relatively uniform. As the laser approaches the Ag line, the Si peak intensity starts to decrease. Once the laser is atop the Ag line, the Si peak disappears completely, as expected. Our region of interest is in the transition region where the Si peak intensity gradually decreases. Here, we note that since the laser spot during the raster does not overlap with the previous spot, the information obtained at any given XY coordinate is expected to be free of neighboring site effects and thus, signal deconvolution is not needed. The drop in intensity of Si can thus be attributed to compositional changes occurring at the site of interest.

The drop in Si peak intensity is attributed to residual Ag_2O on the surface which absorbs part of the laser intensity. The region is highlighted in Fig. 4(b) as an “oxide zone,” This is not unreasonable since Ag_2O has a band gap of $\sim 2.50\text{ eV}$ [25] and is likely to absorb a certain fraction of photons at a wavelength of 532 nm (i.e., photons with energy, 2.33 eV).

To establish the idea of an oxide (i.e., Ag_2O) zone which is wider than the Ag line, we plot the Ag_2O peak intensity as an area map in Fig. 4(c). The dotted lines indicate the edges of the Ag finger and, where the Si peak intensity reaches zero. Clearly, the Ag_2O is detected well beyond the Ag line. Additionally, in Fig. 4(d) we highlight the 3-D optical profilometry results of the Ag line. The oxide zone appears as a discolored region neighboring the Ag line.

A line scan is conducted on the Ag line as indicated in Fig. 4(d). The data is plotted in Fig. 4(e). As mentioned previously, the Si peak intensity drops while approaching the Ag line. Simultaneously, the Ag_2O peak intensity increases in value. Along the Ag line, where the Si intensity is nearly zero, the Ag_2O peak intensity varies depending on the thickness of oxidized Ag on the surface of the finger.

We use the following approach to estimate the thickness of the Ag_2O left behind in the oxide zone. First, we assume that the Si peak intensity is a linear function of the laser intensity [26]. That is, the drop in the Si peak intensity is directly proportional to a corresponding drop in the laser intensity. Thus

$$\frac{I_{\text{Raman}, Si}^{\text{max}}}{I_{\text{laser}}^o} = \frac{I_{\text{Raman}, Si}}{I_{\text{laser}}} \quad (1)$$

where, $I_{\text{Raman}, Si}^{\text{max}}$ is the maximum Raman intensity of Si obtained at a laser intensity of I_{laser}^o (30 mW), $I_{\text{Raman}, Si}$ is the Raman intensity of Si at a given coordinate XY with laser

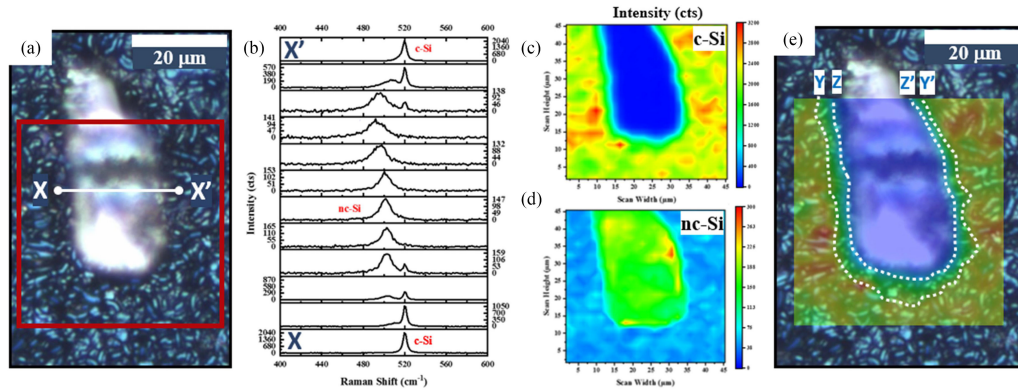


Fig. 5. (a) Microscope image of inclusion with XX' showing the line scan and red box indicating the area scan. (b) Series of twelve spectra taken across XX' showing the transition from c-Si to nc-Si and back to c-Si. (c) XY mapping of the peak intensity for c-Si. (d) XY mapping of the peak position for nc-Si. (e) c-Si peak intensity from (c) overlaid on the microscope image from (a) showing the interfacial region between YY' and ZZ' .

intensity $I_{\text{laser}} (< 30 \text{ mW})$. According to (1), if the laser intensity decreases due to absorption from an overlying film there will be a proportional decrease in the Si Raman peak intensity.

We further assume the drop in laser intensity is due to absorption in the Ag_2O layer. This allows one to apply Beer-Lambert's law to estimate the thickness of Ag_2O film (“ z ”) in the oxide zone. This is given as

$$I_{\text{laser}} = I_{\text{laser}}^o e^{-\alpha z} \quad (2)$$

where α is the absorption coefficient and z is the thickness of the oxide. In (2), I_{laser} is obtained from (1). To apply Beer-Lambert's law to estimate z , the absorption coefficient of Ag_2O at 532 nm must be known. Unfortunately, in literature the absorption coefficient of Ag_2O is rather uncertain. Heat-treated Ag_2O films have an absorption coefficient at 532 nm in the range 0.00078 to 0.00122 nm^{-1} [27]. Thus, these two values serve as the upper and lower limit of the absorption coefficient. Because of the range of the absorption coefficient, the estimated thickness z of the Ag_2O film can, at best, be estimated within a range. The result of this approach is shown in Fig. 4(f). For clarity of understanding, the original Ag_2O Raman peak intensity is plotted again on the left- Y axis and is the same data plotted in Fig. 4(e). This plot provides the $I_{\text{Raman}, \text{Si}}^{\text{max}}$ (at large distances from the Ag line edge) and $I_{\text{Raman}, \text{Si}}$. Overlaid on this plot are the estimated Ag_2O film thickness range as obtained using the upper and lower values of absorption coefficient from (2). The thickness data shows that up to $\sim 200 \text{ nm}$ of Ag_2O can be found 25 μm away from Ag lines.

One possible reason for the presence of the Ag_2O up to 25 μm away from the lines could be the initial application of Ag paste during the screen-printing process. The Ag paste application may have a lateral spread greater than the targeted line width ($\sim 30 \mu\text{m}$) obtained after the firing step. During the firing process, the volatile components are removed from the paste while the metallic components sinter and shrink laterally leaving residual Ag_2O behind.

In supporting information S2, we provide the scanning electron microscope energy dispersive X-ray spectroscopy (SEM EDX) data of a similar, Ag line with elemental mapping. Of particular interest is the O- map which clearly detects O beyond

the width of the Ag line. In supporting information S3, X-ray photoelectron spectroscopy (XPS) of the Ag line is presented, showing a Ag^+ shoulder on the 3-D peaks. XPS indicates 2.24 at % oxide on the surface of Ag lines [28]. These data add further support to the claim of detecting Ag_2O on multicrystalline Si surfaces using Raman.

Fig. 5(a) shows a micrograph of an inclusion as seen under the Raman microscope. This inclusion is previously shown in Fig. 1(e) and (f) as profilometry images. Recall that the 3-D image appears to show this inclusion embedded inside the multicrystalline Si surface. A line scan was conducted from $X \rightarrow X'$. In Fig. 5(b), a series of twelve individual Raman spectra are sampled from X (at the bottom) to X' (at the top). Each scan is 1.6 μm apart. At point X just outside the inclusion, the scan consists of a sharp peak at 520.3 cm^{-1} assigned to crystalline Si (c-Si). As the scan position moves over the inclusion, an additional broad peak appears on the lower wavenumber side. As the probe moves over the inclusion the peak position changes from 504.0 to 492.0 cm^{-1} . Approaching X' , the broad peak subsides, and the c-Si peak sharpens again.

Peak shifts to lower wavenumbers in the TO phonon mode of the Si result from tensile stress, phonon confinement due to nanocrystallinity or, temperature changes to the sample. In the case of nanocrystalline Si (nc-Si), these effects are complex. We identify the secondary Si peak belonging to nc-Si which lies between c-Si (520.3 cm^{-1}) and the fully amorphous Si (a-Si) peak at 480.0 cm^{-1} [29], [30]. Based on past work, the inclusion represents an Si swarf—a possible remnant of the Si ingot sawing process [21], [31]. Here, the c-Si is converted to nc-Si due to the extreme stresses involved during sawing.

To confirm the presence of the nc-Si phase, the Raman peak intensity was measured as a function of the laser power for, c-Si adjacent to the inclusion, and the nc-Si inside the inclusion. This data is shown in supporting information S4. For c-Si, the peak position and FWHM does not vary as laser power varies from 0.87 to 24.3 mW. This is expected since, as shown in supporting information S1, the temperature rise at 10 mW in Si is negligible. On the other hand, the peak position and FWHM of nc-Si is a strong function of laser power. At very low laser

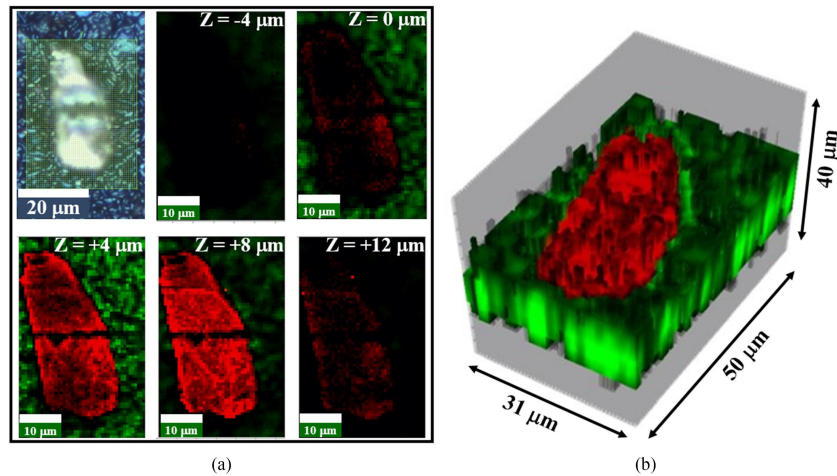


Fig. 6. (a) Top left shows the microscope image of an inclusion with the scan area used for confocal imaging. Confocal XY scans at various Z depths ($-4 \mu\text{m} \leq Z \leq +12 \mu\text{m}$) of the inclusion are shown. (b) 3-D Raman reconstruction of the inclusion. Note: green region is Si and red region is nc-Si.

power (0.87 mW), the peak position and FWHM match that of c-Si. However, with increasing laser power (4.4 mW and higher), the peak position drops to lower wavenumbers and the FWHM increases.

The decreasing wavenumber of the Raman peak associated with the inclusion can be explained based on the different thermal conductivities (k_s) of c-Si and nc-Si. Room temperature bulk Si k_s is 150 W/m K whereas, recent *ab initio* results matching experimental data indicate nc-Si with 20 nm grain size can exhibit a $k_s = 8.4$ W/m K; a $17.8\times$ reduction compared to bulk c-Si [19], [32]. The difference in thermal conductivity is a result of the high grain boundary scattering of phonons in nc-Si [33] indicating that heat dissipation in nc-Si is significantly reduced, producing higher temperatures as compared to c-Si, under the same laser power. Thus, the peak position and FWHM is a strong function of laser power in nc-Si.

The peak intensity of the c-Si and nc-Si phases at laser power 25 mW is mapped in Fig. 5(c) and (d), respectively. The areal mapping is obtained from the red boxed region in Fig. 5(a). Here, the c-Si peak is found to vary from 520.4 to 519.3 cm^{-1} , indicating tensile stress around the inclusion [20]. The broad nc-Si peak, on the other hand, varies from 511.2 to 492.0 cm^{-1} .

A significant aspect of these areal maps is that the c-Si peak intensity reduces in its value at least $2\text{--}5 \mu\text{m}$ away from the observed physical edge of the inclusion. At the same time, the nc-Si peak intensity increases. Thus, the coordinates for which the c-Si peak intensity reduces, and nc-Si has nonzero peak intensities appear to occupy an area much larger than the physical dimensions of the inclusion.

The above effect cannot be an artifact of measurement at phase boundaries usually associated with raster-based mapping techniques under a microscope. There are two reasons for this. First, the laser spot size of 800 nm (for $10\times$ objective) is less than the width of the observed transition region of $2\text{--}5 \mu\text{m}$. This implies the spatial resolution of the measurement exceeds the feature size observed. Second, the raster step of $1.6 \mu\text{m}$ is programmed to ensure any two neighboring laser spots do not overlap with each other. This avoids signal convolution from neighboring spots.

The peak shift to the lower wavenumber for c-Si indicates tensile stress around the inclusion. While the formula for estimating the stress is known under a biaxial state of stress [20], we refrain from calculating this stress due to the complex shape of the inclusion itself. This transition zone is mapped in Fig. 5(e) over the original microscope image of the inclusion. The region between the borders YY' and ZZ' indicates the region where the c-Si is under tensile stress and suggests that the inclusion consisting of nc-Si interacts strongly with underlying c-Si substrate.

The inclusion described above was subjected to confocal Raman mapping as it provides a nondestructive technique for observing subsurface structure and obtain a 3-D map of the inclusion. Confocal mapping was done with a 785 nm laser that, as stated before in the experimental section, allows for a penetration depth of $10 \mu\text{m}$ and is ideally suited for confocal microscopy in Si. The results are shown in Fig. 6(a) as a series of XY intensity plots for different Z heights. At $Z = -4 \mu\text{m}$, the laser cannot detect any part of the Si solar cell. As the sample height is dropped (i.e., focal plane of the laser raised) by $4 \mu\text{m}$ to $Z = 0 \mu\text{m}$, both the Si substrate and the inclusion can be seen. The green color corresponds to the c-Si peak ($519.0 \text{ cm}^{-1} \leq \omega \leq 520.5 \text{ cm}^{-1}$) while the red corresponds to the nc-Si ($492.0 \text{ cm}^{-1} \leq \omega \leq 511.0 \text{ cm}^{-1}$). Intensities for both Si substrate and the inclusion increase for $Z = +4 \mu\text{m}$ and the inclusion can be clearly seen at this Z height. The dark band through the middle was a result of using a high power from the laser that led to partial damage of the inclusion. Further increasing the height to $Z = +8 \mu\text{m}$ shows the inclusion but does not illuminate the substrate in equal proportion, implying that the focal plane of the laser lies beyond the DOF of the objective and above the Si surface. This observation is in line with the profilometry image [see Fig. 1(e) and (f)] which shows the inclusion to protrude beyond the Si solar cell surface. Furthermore, the confocal data identifies the inclusion as nc-Si. Finally, at $Z = +12 \mu\text{m}$ the laser focal plane is far removed from both the inclusion and the Si substrate and are barely detected via mapping. These individual maps can be vertically stacked and represented as a 3-D image as shown in Fig. 6(b), clearly highlighting a nanocrystalline

inclusion embedded on a Si solar cell surface. Thus, confocal Raman microscopy can be a powerful, nondestructive metrology tool to evaluate features in 3-D as well as probe sub-surface features in Si solar cells.

IV. CONCLUSION

With the aim to highlight the utility of Raman as a characterization tool for Si solar cells, we have conducted Raman microscopy on a multicrystalline Al-BSF solar cell. Four prototypical regions were scanned and analyzed. First, multicrystalline Si surface showed peak positions and FWHM comparable with a single crystalline Si wafer, indicating high crystalline quality of the textured Si solar cell surface; Next, regions with remnant saw marks were observed and, although a clear correlation between the image and Raman peaks were not observed, the peak and FWHM distributions were wider and at higher wavenumbers compared to regions on multicrystalline Si with no saw marks; Raman on Ag fingers indicated that ~ 200 nm thick Ag_2O could be detected up to $25 \mu\text{m}$ away from the line edges—a result of the screen-printing followed by firing process. Finally, an inclusion was characterized on the multicrystalline Si surface with the primary phase identified as nanocrystalline Si. The Si substrate around the inclusion was under tensile stress. Confocal mapping provided a nondestructive, 3-D reconstruction of the inclusion, indicating the inclusion was embedded inside and protruded above the multicrystalline Si surface. Taken together, these results demonstrate the utility of Raman microscopy in obtaining insights into the surface and subsurface quality of Si solar cells, defect detection, and characterization.

REFERENCES

- [1] M. A. Green, E. D. Dunlop, J. Hohl-Ebinger, M. Yoshita, N. Kopidakis, and X. Hao, "Solar cell efficiency tables (version 56)," *Prog. Photovolt., Res. Appl.*, vol. 28, no. 7, pp. 629–638, 2020.
- [2] K. Yamamoto, K. Yoshikawa, H. Uzu, and D. Adachi, "High-efficiency heterojunction crystalline Si solar cells," *Jpn. J. Appl. Phys.*, vol. 57, 2018, Art. no. 08RB20.
- [3] D. Quansah, M. Adaramola, G. Takyi, and I. Edwin, "Reliability and degradation of solar PV modules—Case study of 19-year-old polycrystalline modules in Ghana," *Technologies*, vol. 5, no. 2, pp. 22–40, 2017, doi: 10.3390/technologies5020022.
- [4] "Annual Energy Outlook 2020, U.S. energy information administration (EIA), office of energy analysis," U.S. Department of Energy, Washington, DC, USA, 2021, [Online]. Available: <https://www.eia.gov/aeo>
- [5] L. C. Andreani, A. Bozzola, P. Kowalczewski, M. Liscidini, and L. Redorici, "Silicon solar cells: Toward the efficiency limits," *Adv. Phys., X*, vol. 4, no. 1, 2019, Art. no. 1548305.
- [6] R. W. Miles, "Photovoltaic solar cells: Choice of materials and production methods," *Vacuum*, vol. 80, no. 10, pp. 1090–1097, 2006.
- [7] W. Durisch, J. Urban, and G. Smestad, "Characterisation of solar cells and modules under actual operating conditions," *Renewable Energy*, vol. 8, nos. 1–4, pp. 359–366, 1996.
- [8] J. H. Parker, D. W. Feldman, and M. Ashkin, "Raman scattering by Silicon and Germanium," *Phys. Rev.*, vol. 155, no. 3, pp. 712–714, 1967.
- [9] G. Kolb, T. Salbert, and G. Abstreiter, "Raman-microprobe study of stress and crystal orientation in laser-crystallized silicon," *J. Appl. Phys.*, vol. 69, no. 5, pp. 3387–3389, 1991.
- [10] T. C. Damen, S. P. S. Porto, and B. Tell, "Raman effect in zinc oxide," *Phys. Rev.*, vol. 142, no. 2, pp. 570–574, 1966.
- [11] D. Caffrey *et al.*, "Crystallographic characterisation of ultra-thin, or amorphous transparent conducting oxides—The case for Raman spectroscopy," *Materials*, vol. 13, no. 2, pp. 267–281, 2020, doi: 10.3390/ma13020267.
- [12] K. Fleischer *et al.*, "Raman spectra of p-type transparent semiconducting $\text{Cr}_2\text{O}_3:\text{Mg}$," *Thin Solid Films*, vol. 594, pp. 245–249, 2015.
- [13] O. Hollricher and W. Ibach, "High-Resolution optical and confocal microscopy," in *Confocal Raman Microscopy*, Berlin, Germany: Springer, 2010.
- [14] A. J. Beinert *et al.*, "Enabling the measurement of thermomechanical stress in solar cells and PV modules by confocal micro-Raman spectroscopy," *Sol. Energy Mater. Sol. Cells*, vol. 193, pp. 351–360, 2019.
- [15] P. Gundel *et al.*, "Micro-spectroscopy on silicon wafers and solar cells," *Nanoscale Res. Lett.*, vol. 6, no. 1, pp. 197–205, 2011, doi: 10.1186/1556-276x-6-197.
- [16] V. Pogue, S. N. Melkote, and S. Danyluk, "Residual stresses in multicrystalline silicon photovoltaic wafers due to casting and wire sawing," *Mater. Sci. Semicond. Process.*, vol. 75, pp. 173–182, 2018.
- [17] M. Becker, H. Scheel, S. Christiansen, and H. P. Strunk, "Grain orientation, texture, and internal stress optically evaluated by micro-Raman spectroscopy," *J. Appl. Phys.*, vol. 101, no. 6, 2007, Art. no. 063531.
- [18] A. G. Martin and M. J. Keever, "Optical properties of intrinsic silicon at 300 K," *Prog. Photovolt., Res. Appl.*, vol. 3, pp. 189–192, 1995.
- [19] S. Périchon, V. Lysenko, B. Remaki, D. Barbier, and B. Champagnon, "Measurement of porous silicon thermal conductivity by micro-Raman scattering," *J. Appl. Phys.*, vol. 86, no. 8, pp. 4700–4702, 1999.
- [20] I. De Wolf, H. E. Maes, and S. K. Jones, "Stress measurements in silicon devices through Raman spectroscopy: Bridging the gap between theory and experiment," *J. Appl. Phys.*, vol. 79, no. 9, pp. 7148–7156, 1996.
- [21] S. Banerjee *et al.*, "Phase and stress evolution of Si swarf in the diamond-coated wire sawing of Si ingots," *Int. J. Adv. Manuf. Technol.*, vol. 89, nos. 1–4, pp. 735–742, 2016.
- [22] C.-B. Wang, G. Deo, and I. E. Wachs, "Interaction of polycrystalline silver with oxygen, water, carbon dioxide, ethylene, and methanol: In situ Raman and catalytic studies," *J. Phys. Chem. B*, vol. 103, no. 27, pp. 5645–5656, 1999.
- [23] S. Wu *et al.*, "Investigation of the mechanism of the Ag/SiNx firing-through process of screen-printed silicon solar cells," *RSC Adv.*, vol. 4, no. 46, pp. 24384–24388, 2014.
- [24] T. Matsuda, K. Inami, K. Motoyama, T. Sano, and A. Hirose, "Silver oxide decomposition mediated direct bonding of silicon-based materials," *Sci. Rep.*, vol. 8, no. 1, 2018, Art. no. 10472.
- [25] A. J. Varkey and A. F. Fort, "Some optical properties of silver peroxide (Ag_2O) and silver oxide (Ag_2O) films produced by chemical-bath deposition," *Sol. Energy Mater. Sol. Cells*, vol. 29, no. 3, pp. 253–259, 1993.
- [26] T. Nikitin, S. Novikov, and L. Khriachtchev, "Giant raman gain in annealed silicon-rich silicon oxide films: Measurements at 785 nm," *Appl. Phys. Lett.*, vol. 103, no. 15, pp. 151110–151114, 2013, doi: 10.1063/1.4824732.
- [27] S. Banerjee, A. K. Maity, and D. Chakravorty, "Quantum confinement effect in heat treated silver oxide nanoparticles," *J. Appl. Phys.*, vol. 87, no. 12, pp. 8541–8544, 2000, doi: 10.1063/1.373575.
- [28] F. Li *et al.*, "Correlation of UV fluorescence images with performance loss of field-retrieved photovoltaic modules," *IEEE J. Photovolt.*, vol. 11, no. 4, pp. 926–935, Jul. 2021.
- [29] M. S. G. Mohammed, E. Cazzanelli, A. Fasanella, and M. Castriota, "Silicon nanocrystals on the surface of standard Si wafers: A micro-Raman investigation," *J. Mater. Sci. Chem. Eng.*, vol. 6, no. 7, pp. 104–116, 2018.
- [30] Z. Sui, P. P. Leong, I. P. Herman, G. S. Higashi, and H. Temkin, "Raman analysis of light-emitting porous silicon," *Appl. Phys. Lett.*, vol. 60, no. 17, pp. 2086–2088, 1992.
- [31] J. Yang, S. Banerjee, J. Wu, Y. Myung, O. Rezvanian, and P. Banerjee, "Phase and stress evolution in diamond microparticles during diamond-coated wire sawing of Si ingots," *Int. J. Adv. Manuf. Technol.*, vol. 82, nos. 9–12, pp. 1675–1682, 2015.
- [32] L. Yang and A. J. Minnich, "Thermal transport in nanocrystalline Si and SiGe by AB initio based Monte Carlo simulation," *Sci. Rep.*, vol. 7, Mar. 2017, Art. no. 44254.
- [33] Z. Wang, J. E. Alaniz, W. Jang, J. E. Garay, and C. Dames, "Thermal conductivity of nanocrystalline silicon: Importance of grain size and frequency-dependent mean free paths," *Nano Lett.*, vol. 11, no. 6, pp. 2206–2213, Jun. 2011.